Tight-binding models for the iron-based superconductors

Helmut Eschrig* and Klaus Koepernik
IFW Dresden, P.O. Box 270116, D-0111171 Dresden, Germany
(Received 29 May 2009; revised manuscript received 21 July 2009; published 8 September 2009)

The rich materials class of iron-based superconductors turned out to exhibit a very complex electronic structure despite the simplicity of their crystal structures. For various approaches to study the instability against magnetic order or superconductivity, a real-space description of the electronic structure is required. Here, the bonding situation and the orbital structure of the electronic state are analyzed and minimum tight-binding models quantitatively correctly describing the low-energy electronic structure are provided.

DOI: 10.1103/PhysRevB.80.104503 PACS number(s): 74.25.Jb, 74.70.Dd, 71.20.−b

I. INTRODUCTION

The discovery of high-temperature superconductivity in La(O,F)FeAs (Ref. 1) immediately raised great expectations to advance the theory of high-temperature superconductivity in general, since the crystal structure appeared quite simple and on a first glance displayed similarity to that of the cuprates. It quickly turned out, however, that there are also striking differences, in particular of the correlated nature of the electron state. The analysis of many problems in this respect demands real space approaches based on tight-binding (tb) models. An early paper in this direction used a two-orbital tb model.[2] The need for gradually improving such models was already clearly seen in this paper. Unfortunately, improvements turned out to grow terribly in complexity and hopping matrix elements up to the fifth neighbor matter.[3] The situation clearly calls for a detailed analysis of the electronic structure in the tb language as complete as possible. The present paper tries to contribute to this task.

Among the iron-based superconducting materials there are essentially four structural families christened 11, 111, 1111, and 122 according to their stoichiometry in the undoped cases. FeSe and FeTe are representatives of the first family,[4] LiFeAs and NaFeAs represent the second,[5] REOFePN, where RE is Y, La or a light rare-earth element and PN is P, As or Sb, belong to the third,[2,6] and AFe_2As_2, where A is Ca, Sr or Ba, belong to the last.[7] All families exhibit a tetragonal structure at room temperature which slightly distorts below the Néel temperature of the antiferromagnetic order. The first three families have the nonsymmorphic space group $P4/nmm$ in common, while the last family crystallizes in the symmorphic space group $I4/mmm$. The unit cells of the first three families as well as the tetragonal cell of the last (which contains two unit cells) are shown in Fig. 1.

The generic structural element is a metallic iron chalcogenide/pnictide layer consisting of a square iron atom plane sandwiched between two chalcogen/pnictogen (c/p) atom planes in such a way that every Fe atom is in the center of a c/p tetrahedron. The families 11 and 111 consist of neutral metallic layers only, stacked on top of each other in the direction of the tetragonal axis and only weakly bonded in this direction. Thereby LiAs is isoelectronic with Se. They should easily cleave in planes perpendicular to the tetragonal axis. In contrast, in the 1111 and 122 families the FeAs layer is charged and anionic and is intercalated with a nonconducting cationic layer, e.g., LaO in the 1111 family and Ba in the 122 family. Hence, these materials cannot neutrally cleave between intact atom layers.

Phenomenologically, superconductivity seems to be quite robust in the (doped) families 1111 and 122, but more sensitive to imperfections in the families 11 and 111. This at least goes in line with a remarkable structural difference revealed in Table I. For representatives of the four families this table shows the nearest in-plane Fe-Fe distance d in Å, and the ratio r of the distance of c/p layers from the Fe layer related to the in-plane Fe-Fe distance. This latter ratio would be 0.5 in the case of regular c/p tetrahedra. As is evident from Table I, the cationic interlayers of the 1111 and 122 families put the Fe layer under considerable tensile strain and in line with that the c/p tetrahedra are considerably contracted in the direction of the tetragonal axis. The ratio r is by the way unusually badly reproduced by lattice relaxation within nonmagnetic density-functional theory (DFT) and it seems to be somewhat sensitive to magnetic order. Which of the Fe $3d$ bands cross the Fermi level and the sequence in energy of these bands depends on the actual value of r and often differs for the experimental value and for the DFT relaxed value.

All results presented in this paper refer to the experimental structure data and to the nonmagnetic state.

The aim is to provide tb models of the low-energy background electronic structure on the basis of which collective behavior such as magnetism and superconductivity may develop and may be analyzed by many-body theories. It will be shown that the low-energy physics is essentially more two-dimensional (2D) in the families 1111 and 122 than in the other two, again distinguishing the lower two families of Table I from the upper two.

In Fig. 2 the essential atomic-shell resolved partial densities of states (DOS) together with the total DOS are shown for the experimental structure parameters of FeSe (a =3.7734 Å, c=5.5258 Å, z_{Se}=0.267, z_{Fe}=0).[8] All band structures in this work are obtained with the high precision full-potential local orbital code FPLO8 (Ref. 9) using the Perdew-Wang 92 (Ref. 10) version of the local-density approximation (LDA) density functional. Generalized gradient approximation (GGA) results would somewhat differ in the lattice relaxation by total energy minimization. Since, however, for given fixed structural parameters the results considered here hardly differ at all, and all results presented in this text are for the experimental structures, LDA was used throughout.

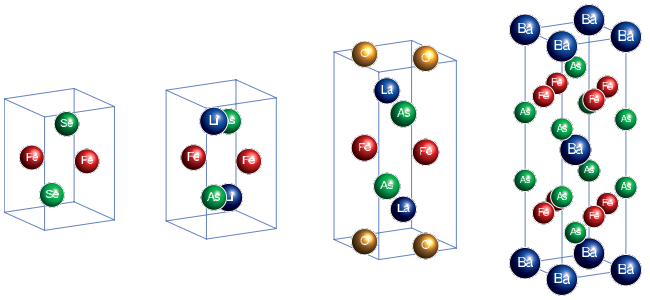

FIG. 1. (Color) From left to right: unit cells of FeSe, LiFeAs, LaOFeAs, and $BaFe_2AS_2$ (the tetragonal cell contains two unit cells in the latter case).

For what follows it is relevant that the all-electron approach FPLO8 uses a carefully optimized "chemical" basis (one basis orbital per atomic core or valence orbital) plus at most one polarization orbital per band. The quality of the chemical basis results in occupation numbers of polarization orbitals usually well below 0.02 (per spin), in most cases even much lower (without loss in accuracy which competes with any of the advanced all-electron full-potential tools presently available. For instance, in a recently published work[11] results for the 1111 compound LaOFeAs obtained with different band structure methods were compared and very good agreement between FPLO and FPLAPW results was assessed. This is the reason why projections on the FPLO chemical basis orbitals have a lot of chemical relevance, and also produce nearly optimally localized Wannier orbitals from band structures in an approach described below in Sec. IV.

The situation shown in Fig. 2 which is generic for all four families considered here can be understood as follows: since there are two Fe atoms per unit cell, there is Fe-Fe homocovalency. Put the structural layers in the xy plane stacked in z direction. For zero wave vector there are in-plane bonding combinations of Fe $3d$ orbitals with angular dependence xy/r^2 and $(x^2-y^2)/r^2$, respectively, with the same coefficient on both sites and antibonding combinations with sign-alternating coefficients. For the angular dependence xz/r^2 and yz/r^2 it is just the other way round, while the orbitals $\sim(z^2/r^2-3)$ form essentially nonbonding bands. Hence, there are four Fe-Fe bonding bands, four Fe-Fe antibonding bands, and two nonbonding bands. The Se $4p$ orbitals may couple with the Fe-Fe antibonding combinations only, developing Fe-Se heterocovalency with predominantly Se $4p$ bands below -3 eV and predominantly Fe $3d$ bands above the Fermi level (the latter put at zero-band energy). The

TABLE I. Structural parameters of the four families as described in the text.

Family	Representative	d	r
11	FeSe	2.6653	0.5350
111	LiFeAs	2.6809	0.5614
1111	LaOFeAs	2.8497	0.4620
122	$BaFe_2As_2$	2.8019	0.4855

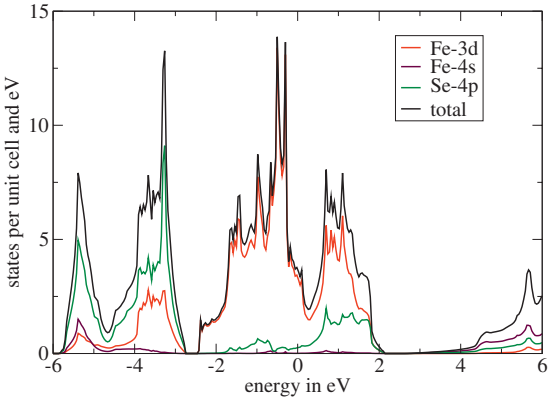

FIG. 2. (Color) Partial and total DOS for FeSe. The Fermi level is at 0 eV.

Fermi level itself falls in a Fe-Fe covalency pseudogap between the bonding plus nonbonding bands of essentially pure Fe $3d$ character and the antibonding bands of hybridized Fe $3d$-Se $4p$ character. This picture prevails in large parts of the Brillouin zone (BZ) and only modifies in the vicinity of the BZ edges parallel to the z axis (through point M of Fig. 9 below). It results in rather small hole Fermi surfaces (FS) of Fe-Fe bonding bands around the k_z axis and in likewise small electron FS around the BZ edges parallel to this axis, and hence in the pseudogap at the Fermi level. The materials are not far from semimetals.

There is also Fe $4s$-Se $4p$ covalency with a gap of about 7 eV as seen on the bottom of Fig. 2. The modifications in the other families compared to 11 are gradual, see Figs. 3–5. Since the As $4p$ states are about 1 eV higher than the Se $4p$ states, the gap below -2 eV is less pronounced or absent in the arsenides. In LiFeAs the pseudogap at the Fermi level is less pronounced too as the Fermi radii are somewhat larger (larger energy overlap between Fe-Fe bonding and antibonding band groups). In LaOFeAs and $BaFe_2As_2$ there is also no gap above 2 eV as the La $4f$ states and the Ba $5d$ states, respectively, come down close to the Fermi level. (About 0.4 Ba $5d$ states are occupied in $BaFe_2As_2$ while, when doping with K, the K $3d$ states remain empty; this is why one K atom when replacing Ba donates only about 0.6 holes or 0.3 holes per Fe atom into the Fe $3d$ bands.) Moreover, the O $2p$

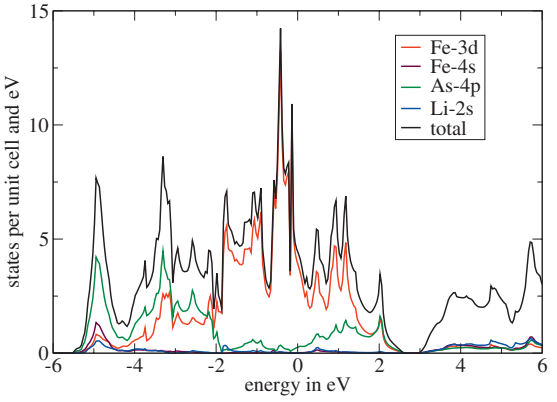

FIG. 3. (Color) Partial and total DOS for LiFeAs. Experimental structure parameters from Ref. 12.

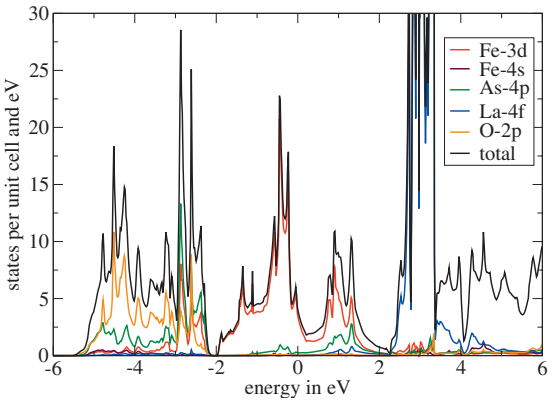

FIG. 4. (Color) Partial and total DOS for LaOFeAs. Experimental structure parameters from Ref. 13.

states of LaOFeAs appear below −2 eV in addition to the As 4*p* states. In the range between −2 eV and the Fermi level there is not so much difference in the bands being almost purely Fe 3*d* in all cases.

The whole situation with Fe 3*d*-Fe 3*d* and Fe 3*d*-c/p-4*s* covalency is illustrated for the generic example of FeSe in Fig. 6. The projection of the LDA bands on the FPLO chemical basis orbitals is given as line thickness in color code. (The diameter of the color balls in the legend of the figure indicates the thickness for 100 percent orbital content in the band wave function.) The cyan (c/p-*pz*) band on the line Γ-*Z* which disperses down close to the Fermi level has a black component (Fe *xy*) hidden behind the cyan and amounting to about half of the band state near *Z*. The narrowness below the Fermi level of the nonbonding Fe z^2 bands is clearly seen. Again seen is that the Fe-Fe bonding bands below the Fermi level do not hybridize with the c/p-4*p* orbitals while Fe-Fe antibonding bands strongly hybridize. Due to the far extend of the radial orbitals, the c/p-4*p* states extend even above the Fe 3*d* bands, over an energy range of more than 10 eV. It is also seen that the Fermi level is crossed by Fe *xy*, *xz*, and *yz* bands only with a small admixture of c/p4*pz* orbitals. Right below Fermi level Fe x^2-y^2 and z^2 admixture sets in, so that one fails to reproduce Fermi velocities even qualitatively without consideration of the latter orbitals and their corresponding bands.

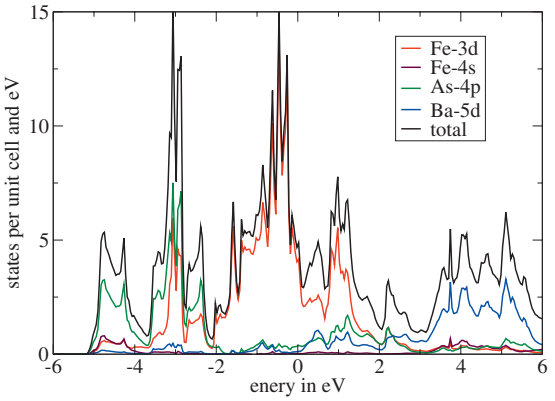

FIG. 5. (Color) Partial and total DOS for $BaFe_2As_2$. Experimental structure parameters from Ref. 14.

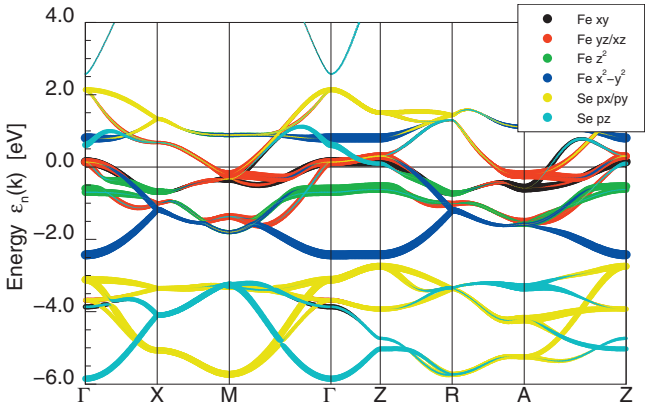

FIG. 6. (Color) Orbital projection of the LDA band structure of FeSe. (See Fig. 9 for the points Γ, *X*, *M*; *Z*, *R*, and *A* are above the former at $k_z=\pi$.)

Remarkable in this respect is also the orbital anisotropy of the FS, again in stark contrast to the case of the cuprates. While the three FS hole cylinders around Γ-*Z* appear more or less orbitally isotropic with one of the outer cylinders and the inner cylinder of $xz-yz$ character (of course with their mixing rotating together with $\boldsymbol{k}$) and the other outer cylinder of *xy* character, the outer FS electron cylinder around M in the $k_z=0$ plane appears totally orbitally anisotropic with $xz-yz$ character in the directions toward *X* and nearly pure *xy* character in the directions toward Γ. The inner electron cylinder is again more or less orbitally isotropic with $xz-yz$ character. In the $k_z=\pi$ plane the inner and outer electron cylinders have interchanged their orbital character.

In all those considerations the presence of the c/p atoms is essential. Without there presence, the unit cell would reduce to containing one Fe atom only, and no interband Fe-Fe covalency could develop. In Fig. 7 the DOS of a hypothetical lattice is shown with the Se atoms removed from the FeSe crystal, but the Fe atoms left at their positions. The Fe 3*d* occupation remains nearly the same (Mullikan analysis with the FPLO8 basis results in charge transfer between Fe and c/p of less than 0.1 electron charge/atom), but no pseudogap whatsoever appears as there are now only five Fe 3*d* bands in the doubled BZ. There is also no covalency band gap of the Fe-4*s* states any more. Fe-Fe covalency appears only due to

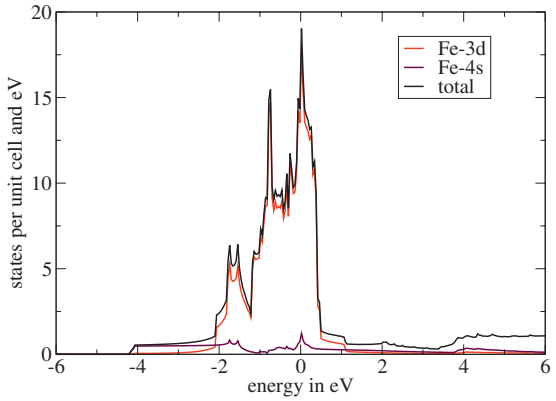

FIG. 7. (Color) Partial and total DOS for a hypothetical structure obtained by removing the Se atoms from FeSe.

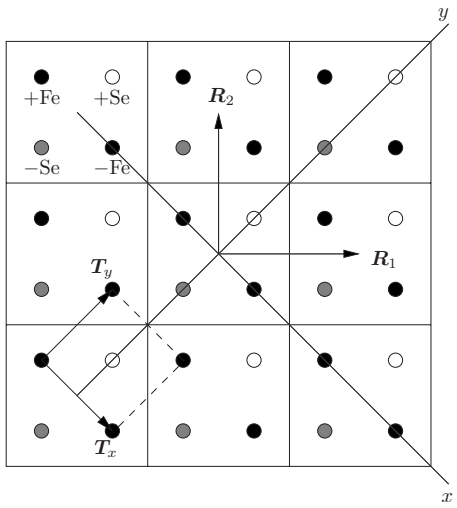

FIG. 8. Tetragonal plane of nine unit cells (full-line squares) spanned by lattice basis vectors $\boldsymbol{R}_1$ and $\boldsymbol{R}_2$ of FeSe. The open circles mark Se positions above and the shadowed circles below the drawing plane. The Fe sites (full circles) are located in the drawing plane. If the Se sites are neglected, the half-size unit cell is spanned by $\boldsymbol{T}_x$ and $\boldsymbol{T}_y$ as shown in the left lower corner.

the doubling of the unit cell caused by the presence of the c/p atoms, due to their additional potential and due to hybridization with c/p-p orbitals. Also, the width and depth of the pseudogap are quite sensitive to the c/p position, that is, to the actual value of the Wyckoff parameter $z_{\mathrm{c/p}}$.

In a vicinity of half an eV around the Fermi level, the band structure in the 1111 family exhibits a pronounced quasi-2D character. It is somewhat less 2D and in a narrower energy window at the Fermi level in the 122 family and much more three-dimensional (3D) in the 11 and 111 families.

In the next section the implications of symmetry on the electronic structure are analyzed in detail. This provides some key to the construction of reduced tb models. In Sec. III, a minimum 2D tb model is derived for reasonable quantitative approximations of the low-energy band structures of the Fe-c/p layers (the focus being essentially on excitation energies below 0.1 eV) and parameters are given for representatives of all four families. These are based on a Wannier function representation introduced in Sec. IV. The families 11 and 111 exhibit quite sizable 3D dispersion close to the Fermi level. Corresponding 3D tb models for these cases are given in Sec. V and finally the results are summarized in Sec. VI.

II. SYMMETRY OF THE IRON CHALCOGENIDE/ PNICTIDE LAYER

The 11 family consists of the Fe-c/p layers only generic for all four families. To be specific, FeSe is taken as example in what follows. We start with a more detailed description of the FeSe structure.

The two Fe and Se positions per unit cell are symbolically distinguished by a sign. Atom positions are (Fig. 8)

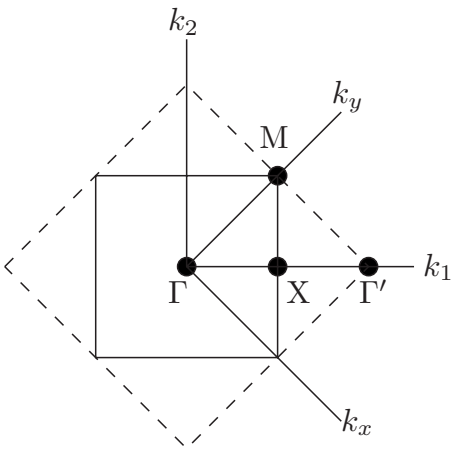

FIG. 9. BZ of the structure of Fig. 8, dashed for the Fe structure alone (one Fe atom per cell) and full lines for the full FeSe structure. The wave-number components are scaled so that the symmetry points are $(k_x,k_y)=(0,0)$ for Γ, $(\pi/2,\pi/2)$ for X, $(\pi,0)$ for M, and (π,π) for Γ', as well as $(k_1,k_2)=(0,0)$ for Γ, $(\pi,0)$ for X, (π,π) for M, and $(2\pi,0)$ for Γ'.

$$\boldsymbol{S}_{\pm\mathrm{Fe}}=\frac{1}{4}(\mp\boldsymbol{R}_1\pm\boldsymbol{R}_2),$$

$$\boldsymbol{S}_{\pm\mathrm{Se}}=\frac{1}{4}(\mp\boldsymbol{R}_1\mp\boldsymbol{R}_2)\pm z_{\mathrm{Se}}\boldsymbol{R}_3. \tag{1}$$

The vectors $\boldsymbol{T}_x$ and $\boldsymbol{T}_y$ of Fig. 8 are not lattice vectors of the full structure. However, in combination with a reflection n on the (x,y) plane they nevertheless form nonsymmorphic symmetry elements $(n|\boldsymbol{T}_x)$, $(n|\boldsymbol{T}_y)$ [diagonal glide plane, $(n|\boldsymbol{T}_x)\phi(\boldsymbol{r})=\phi(n^{-1}\boldsymbol{r}-\boldsymbol{T}_x)$, $n^{-1}=n$]. Applied to a Bloch state $\psi_{\boldsymbol{k}\nu}(\boldsymbol{r})$, any space group element yields $(A|\boldsymbol{T}_A+\boldsymbol{R}_l)\psi_{\boldsymbol{k}\nu}(\boldsymbol{r})=\exp[i(A\boldsymbol{k})\cdot\boldsymbol{R}_l]\psi'_{A\boldsymbol{k}}(\boldsymbol{r})$, where ν is the band index and $\psi'_{A\boldsymbol{k}}(\boldsymbol{r})$ is a linear combination of states $\psi_{A\boldsymbol{k}\nu'}(\boldsymbol{r})$ with the restriction $\varepsilon_{A\boldsymbol{k}\nu'}=\varepsilon_{\boldsymbol{k}\nu}$ on the band energies. [$\boldsymbol{T}_n=\boldsymbol{T}_x$, some one-one relation $A\leftrightarrow\boldsymbol{T}_A$ must be chosen, $(n|\boldsymbol{T}_y)=(n|\boldsymbol{T}_n+\boldsymbol{R}_2)$. Moreover, the result of $(A|\boldsymbol{T}_A+\boldsymbol{R}_l)\psi_{\boldsymbol{k}\nu}(\boldsymbol{r})$ is based on a chosen phase relation between $\psi_{\boldsymbol{k}\nu}(\boldsymbol{r})$ and $\psi'_{A\boldsymbol{k}}(\boldsymbol{r})$, which choice is made here for the sake of simplicity different from that later in Eqs. (10) and (16); the results considered here do not depend on this choice.] One has $(A|\boldsymbol{T}_A)(B|\boldsymbol{T}_B)=(AB|\boldsymbol{T}_{AB}+\boldsymbol{R}_{AB})$, where $\boldsymbol{R}_{AB}$ is a lattice vector. If, for the wave-vector group of $\boldsymbol{k}$, $\{(A|\boldsymbol{T}_A+\boldsymbol{R}_l)|A\boldsymbol{k}=\boldsymbol{k}+\boldsymbol{G}_A\}$ where $\boldsymbol{G}_A$ is a reciprocal lattice vector, one defines the multiplier representation $\rho^A_{\nu'\nu}(\boldsymbol{k})=\exp(-i\boldsymbol{k}\cdot\boldsymbol{R}_l)\langle\psi_{\boldsymbol{k}\nu'}|(A|\boldsymbol{T}_A+\boldsymbol{R}_l)|\psi_{\boldsymbol{k}\nu}\rangle$, then

$$\rho^A\rho^B=\exp(i\boldsymbol{k}\cdot\boldsymbol{R}_{AB})\rho^{AB} \tag{2}$$

follows. Time inversion T is defined as the antiunitary operator $T\phi(\boldsymbol{r})=\phi^*(\boldsymbol{r})$ and hence $T\psi_{\boldsymbol{k}\nu}=\psi_{-\boldsymbol{k}T\nu}$ and $T(A|\boldsymbol{T}_A+\boldsymbol{R}_l)=(A|\boldsymbol{T}_A+\boldsymbol{R}_l)T$. Now, if m_2 is the reflection plane through iron sites sending $\boldsymbol{R}_2\rightarrow-\boldsymbol{R}_2$, then the antiunitary operator $\Theta=Tm_2(n|\boldsymbol{T}_n)$ is an element of the wave vector group for any wave vector $\boldsymbol{k}$ with $\boldsymbol{k}\cdot\boldsymbol{R}_1=\pm\pi$, that is, on the face of the BZ with central point X (Fig. 9), and $\rho^\Theta(\boldsymbol{k})\rho^\Theta(\boldsymbol{k})=-1$ for any such $\boldsymbol{k}$ since $\Theta^2=(1|\boldsymbol{R}_1)$. The existence of an antiunitary operator with square equal to -1 which commutes with the

Hamiltonian is an analog to Kramers degeneracy,[15] and an immediate consequence here is a twofold degeneracy of all bands on the four side faces of the BZ. ($\boldsymbol{R}_1$ and $\boldsymbol{R}_2$ may be interchanged in the above considerations, with m_2 replaced with m_1.) One also has $-[m_1(n|\boldsymbol{T}_n)+(n|\boldsymbol{T}_n)m_1]/2=2_1^2$, $[m_2(n|\boldsymbol{T}_n)+(n|\boldsymbol{T}_n)m_2]/2=2_1^1$, where 2_1^2 is a screw rotation by π around the axis through the lattice vector $\boldsymbol{R}_2$ of Fig. 8, accompanied by a glide by the vector $\boldsymbol{R}_2/2$, and 2_1^1 is the corresponding screw rotation around $\boldsymbol{R}_1$ as given in that figure. The notation of space group elements follows Hermann-Mauguin.[16] We prefer to use the two reflections in the considerations of hopping matrix elements below.

This is all generally true for the $P4/nmm$ space group (which is also the space group of a single FeSe layer of Fig. 8). Hence, it holds for the 11, 111, and 1111 materials (FeSe, LiFeAs, and LaOFeAs as examples). It does not hold for the 122 materials (e.g., $BaFe_2As_2$) which crystallize in the $I4/mmm$ structure (body-centered tetragonal). The space group $I4/mmm$ is symmorphic and hence there appear no multipliers different from unity in representations of wave-vector groups and no twofold degeneracies on whole BZ faces. These degeneracies only reappear, if one neglects z-axis dispersion. In the following we first focus on the layer structure of Fig. 8 which is representative for all four families, if z-axis dispersion is neglected.

The full crystal potential V must be invariant under all symmetry operations including lattice translations and glide reflections. With respect to the latter, it can be decomposed into a part V_+ that is invariant under both the $\boldsymbol{T}_x$ or $\boldsymbol{T}_y$ translations and the reflection n on the (x,y) plane separately and a part V_- that is alternating with respect to both separate operations. This potential representation will be used in the next section.

Further important symmetry transformations of all structures with the $P4/nmm$ space group are a π-rotation 2^x around the x axis of Fig. 8(a) π-rotation 2^y around a parallel to the y axis through Fe sites and the spatial inversion $\bar{1}$ with its center halfway between any of the pairs $\pm X$ of atoms (all pairs have the same midpoint). Nonzero Hamiltonian matrix elements must either be invariant under symmetry transformations of the structure or transform into each other.

Due to the presence of the glide plane $(n|\boldsymbol{T}_n)$, all atom positions within the unit cell of the layer of Fig. 8 or more generally of a crystal with $P4/nmm$ space group come in symmetry equivalent pairs $\pm X$ such as $\pm$Fe and $\pm$Se in Fig. 8. Denote local site orbitals of a local orbital basis correspondingly by a sign superscript as $\phi^{\pm}$. (This superscript is to be well distinguished from the sign subscript on $V_{\pm}$ for the component of the crystal potential which has a different meaning defined above, although related to the same symmetry element.) Expanded in this basis, the Hamiltonian may be brought into a block matrix structure

$$H=\begin{pmatrix} H^{++} & H^{+-} \\ H^{-+} & H^{--} \end{pmatrix}, \tag{3}$$

where, if one denotes hopping matrix elements by t_{ij}^{rst} for hopping a distance $r\boldsymbol{T}_x+s\boldsymbol{T}_y+t\boldsymbol{R}_3$, r,s integer, between local site orbitals ϕ_i and ϕ_j (of either superscript), then hoppings with $r+s$ even (accompanied with corresponding Bloch phase factors) enter H^{++} and H^{--} while hoppings with $r+s$ odd enter H^{+-} and H^{-+}.

Note that the antiunitary transformation $T\bar{1}$ is an element of the wave-vector group for every wave vector $\boldsymbol{k}$, this time with $(\rho^{T\bar{1}})^2=+1$ and, hence, not causing a degeneracy. The local site orbitals may always be chosen so that

$$T\bar{1}\phi^{\pm}=\phi^{\mp}, \tag{4}$$

this time also for the 122 structure, in all cases with respect to the center of inversion $\bar{1}$ half way between nearest Fe neighbors.

For instance, if in a natural way the local site orbitals are parity eigenstates, appropriate imaginary factors at odd parity orbitals do. Then, for the hopping matrix elements one has $\langle\phi^-|\hat{H}|\phi^-\rangle=\langle T\bar{1}\phi^-|\hat{H}|T\bar{1}\phi^-\rangle^*=\langle\phi^+|\hat{H}|\phi^+\rangle^*$ and $\langle\phi^-|\hat{H}|\phi^+\rangle=\langle\phi^+|\hat{H}|\phi^-\rangle^*$. It immediately follows that with this basis choice (which is always possible and even the natural one)

$$H=\begin{pmatrix} H^{++} & H^{+-} \\ H^{+-*} & H^{++*} \end{pmatrix}. \tag{5}$$

Since generally $H^{-+}=H^{+-\dagger}$, it also follows that the block matrix H^{+-} must be symmetric:

$$H^{+-^t}=H^{+-}, \tag{6}$$

where H^t means the transposed of H. This reduces the calculation of Hamiltonian (and overlap) matrix elements by a factor of two.

III. TIGHT-BINDING BANDS FOR THE IRON CHALCOGENIDE/PNICTIDE LAYER

In this section tb models for the iron c/p layers are considered. Again, to be specific, the discussion is first for FeSe and then generalized. Fe $3d$ orbitals are denoted by their angular character and by an upper sign indicating centering at site $\boldsymbol{S}_{\pm\mathrm{Fe}}$ as in the previous section for the general case. For instance $(ixz)^+$ means a real orbital with angular dependence xz/r^2 centered at $\boldsymbol{S}_{+\mathrm{Fe}}$, multiplied with the imaginary unit factor later being used to get real Hamiltonian matrices; (z^2) abbreviates the real orbital with angular dependence $(3z^2-r^2)/r^2$. The following site orbitals $\phi^{\pm}$ within a unit cell are introduced which obey Eq. (4):

$$\begin{aligned} &1:\quad (xy)^+, \quad 6:\quad (xy)^-, \\ &2:\quad (x^2-y^2)^+, \quad 7:\quad (x^2-y^2)^-, \\ &3:\quad (ixz)^+, \quad 8:\quad (-ixz)^-, \\ &4:\quad (iyz)^+, \quad 9:\quad (-iyz)^-, \\ &5:\quad (z^2)^+, \quad 10:\quad (z^2)^-. \end{aligned} \tag{7}$$

The numbering of orbitals will later be used for (lower) matrix indices of the hopping matrices t_{ij}. If in what follows no

superscript is applied, then ϕ means an orbital either on site $\boldsymbol{S}_{+\mathrm{Fe}}$ or on $\boldsymbol{S}_{-\mathrm{Fe}}$.

There are four distinct onsite Hamiltonian diagonal matrix elements [the subscript i being again the number from Eq. (7)]

$$\epsilon_i, \quad \epsilon_4 = \epsilon_3, \quad \epsilon_{i+5} = \epsilon_i, \tag{8}$$

while due to orbital onside orthogonality there are no onside Hamiltonian off-diagonal matrix elements. The 10×10 Hamiltonian matrix in site orbital representation has an obvious 5×5 block structure Eqs. (5) and (6).

Since only one layer is considered, only in-plane hoppings t_{ij}^{rs} a distance $r\boldsymbol{T}_x+s\boldsymbol{T}_y$ figure, a fact relevant in what follows. Now one has to distinguish matrix elements, the orbital products of which are even with respect to reflection on the (x,y) plane and which hence are coupled by the kinetic-energy operator and by V_+, from the ones, the orbital products of which are odd with respect to reflection on the (x,y) plane and which hence are coupled by V_-. The former are (superscripts dropped, $i,j=1,\ldots,5$) t_{ii}, t_{12}, t_{15}, t_{25}, and t_{34} their transposed and the corresponding $t_{i+5,j+5}$, $t_{i,j+5}$, and $t_{i+5,j}$. The latter are t_{ij}, $i=1,2,5$; $j=3,4$ their transposed and the corresponding $t_{i+5,j+5}$, $t_{i,j+5}$, and $t_{i+5,j}$.

For the former one has immediately $t_{i+5,j+5}=t_{ij}$ and $t_{i+5,j}=t_{i,j+5}$, respectively, while for the latter the same relations are the consequence of our phase choices in Eq. (7). With our choice of the orbitals the former matrix elements are real while the latter are purely imaginary. The matrix elements t_{55} and $t_{5,10}$ between the essentially nonbonding orbitals are small and are neglected further on.

Considering the symmetry transformations of the structure it is easily found that the nine distinct nonzero first-neighbor hoppings are $t_{16}^{10}=t_{16}^{\bar{1}0}=t_{16}^{01}=t_{16}^{0\bar{1}}$, $t_{18}^{10}=-t_{18}^{\bar{1}0}=t_{19}^{01}=-t_{19}^{0\bar{1}}$, $t_{27}^{10}=\cdots$, $t_{29}^{10}=-t_{28}^{01}=\cdots$, $t_{2,10}^{10}=\cdots$, $t_{38}^{10}=t_{49}^{01}=\cdots$, $t_{49}^{10}=t_{38}^{01}=\cdots$, and $t_{4,10}^{\bar{1}0}=t_{3,10}^{01}=\cdots$, where we did not spell out all relations which follow rather obviously from the above-mentioned symmetry transformations of the structure and of the orbital products from which also the relations $t_{i,j+5}^{mn}=t_{j,i+5}^{mn}$, $m+n$ odd follow. As an example, one of the above relations, $t_{18}^{10}=-t_{18}^{\bar{1}0}$, is obtained by a π-rotation 2^y which transforms $(xy)^+$ into $-(xy)^+$ and $(ixz)^-$ into itself shifted by a translation $(m,n)=(-2,0)$. $t_{18}^{10}=t_{19}^{01}$ is obtained by an m_2 reflection. As an example of the last mentioned type ($t_{i,j+5}^{mn}=t_{j,i+5}^{mn}$), $t_{18}^{10}=t_{36}^{10}$ is obtained by a π-rotation 2^x changing the sign of the orbital $(xy)^+$ but not that of $(-ixz)^-$, and a subsequent shift by $\boldsymbol{T}_x$ mapping $(xy)^+$ to $(xy)^-$ and $(-ixz)^-$ to $[(ixz)^+]^*$. Since $(ixz)^+$ couples to $(xy)^-$ via V_-, the $\boldsymbol{T}_x$ shift changes the sign of the matrix element back. On the other hand, in $t_{2,10}^{10}=t_{57}^{\bar{1}0}$ no sign change in orbitals happens in the π-rotation 2^y and no sign change in the shift by $\boldsymbol{T}_x$ since this time the orbitals couple via the kinetic-energy operator and V_+.

There are also nine distinct nonzero second-neighbor hoppings t_{ij}^{11}, $i,j=1,\ldots,5$, while $t_{12}^{11}=0$, $t_{25}^{11}=0$, $t_{14}^{11}=t_{13}^{11}$, and $t_{24}^{11}=-t_{23}^{11}$ both latter cases by an m_2 reflection, $t_{44}^{11}=t_{33}^{11}$, $t_{45}^{11}=t_{35}^{11}$, and $t_{ij}^{mn}=t_{ji}^{mn}$, $m+n$ even. For instance for $ij=11$ the latter relations are obtained by an m_1 reflection, and, for i or j or both equal to 3 or 4, by an additional m_2 reflection. As already obtained in the general case, $t_{i+5,j+5}^{11}=t_{ij}^{11}$.

Since we try to limit the number of parameters as much as possible and we focus on the low-energy vicinity of the Fermi level, we neglect t_{55} and $t_{5,10}$ for the Fe-Fe nonbonding bands which stay away from the Fermi level by more than half an eV. (Note, however, that for the LDA or GGA *relaxed* structure parameters these bands may even cross the Fermi level; so far there are nevertheless no reasons to assume that this happens in nature.) The hybridization parameters t_{i5}, $i=1,\ldots,4$ however cannot be neglected. They strongly influence some Fermi velocities.

The hoppings t^{11} happen essentially through the c/p site. Due to the large radial extent of the c/p-4p orbitals, nearest neighbor c/p-c/p hopping along the c/p tetrahedron edges is strong, and hence the effective Fe-Fe hoppings t^{20}, t^{21}, and t^{22} are not yet small. In order to fit besides the FS radii, also the Fermi velocities reasonably well, they must be taken into account at least for the orbitals 1, 3, 4 and 6, 8, 9.

Figure 9 shows the two-dimensional BZ of the FeSe slab of Fig. 8. A notation

$$k_1 = k_x + k_y, \quad k_2 = -k_x + k_y \tag{9}$$

is used and Bloch sums are defined as

$$\phi_{\boldsymbol{k}i} \sim \sum_l \phi_i e^{i\boldsymbol{k}\cdot(\boldsymbol{R}_l+\boldsymbol{S}_i)}, \tag{10}$$

where $\boldsymbol{S}_i$ is the site of the basis orbital ϕ_i.

The Hamiltonian matrix H^{++} in Bloch state representation is

$$H_{11}^{++} = \epsilon_1 + 2t_{11}^{11}(\cos k_1 + \cos k_2) + 2t_{11}^{20}[\cos(2k_1) + \cos(2k_2)],$$

$$H_{12}^{++} = 0,$$

$$H_{13}^{++} = 2it_{13}^{11}(\sin k_1 - \sin k_2),$$

$$H_{14}^{++} = 2it_{13}^{11}(\sin k_1 + \sin k_2),$$

$$H_{15}^{++} = 2t_{15}^{11}(\cos k_1 - \cos k_2),$$

$$H_{22}^{++} = \epsilon_2 + 2t_{22}^{11}(\cos k_1 + \cos k_2),$$

$$H_{23}^{++} = 2it_{23}^{11}(\sin k_1 + \sin k_2),$$

$$H_{24}^{++} = 2it_{23}^{11}(-\sin k_1 + \sin k_2),$$

$$H_{25}^{++} = 0,$$

$$H_{33}^{++} = \epsilon_3 + 2t_{33}^{11}(\cos k_1 + \cos k_2) + 2t_{33}^{20}\cos(2k_x) + 2t_{33}^{02}\cos(2k_y) + 4t_{33}^{22}\cos(2k_x)\cos(2k_y),$$

$$H_{34}^{++} = 2t_{34}^{11}(\cos k_1 - \cos k_2),$$

$$H_{35}^{++} = 2it_{35}^{11}(\sin k_1 + \sin k_2),$$

$$H_{44}^{++} = \epsilon_3 + 2t_{33}^{11}(\cos k_1 + \cos k_2) + 2t_{33}^{02}\cos(2k_x) + 2t_{33}^{20}\cos(2k_y) + 4t_{33}^{22}\cos(2k_x)\cos(2k_y),$$

$$H_{45}^{++} = 2it_{35}^{11}(\sin k_1 - \sin k_2),$$

$$H_{55}^{++} = \epsilon_5,$$

$$H_{ji}^{++} = (H_{ij}^{++})^*. \tag{11}$$

Of course, H^{++} is Hermitian and in agreement with Hermiticity and our phase choice in Eq. (2) one finds that t_{ij}^{11} is real for $t_{ij}^{11} = t_{ji}^{11}$ and imaginary for $t_{ij}^{11} = -t_{ji}^{11}$. Hence, one finds that H_{ij}^{++} is real. Together with Eq. (5) this also implies

$$H^{--} = H^{++}. \tag{12}$$

This reality is the consequence of absence of hoppings in $\boldsymbol{R}_3$ direction and does not hold in the more general case.

For H^{+-} one finds

$$\begin{aligned} H_{16}^{+-} &= 2t_{16}^{10}(\cos k_x + \cos k_y) \\ &+ 2t_{16}^{21}[(\cos k_1 + \cos k_2)(\cos k_x + \cos k_y) \\ &- \sin k_1(\sin k_x + \sin k_y) + \sin k_2(\sin k_x - \sin k_y)], \end{aligned}$$

$$H_{17}^{+-} = 0,$$

$$H_{18}^{+-} = 2it_{18}^{10} \sin k_x,$$

$$H_{19}^{+-} = 2it_{18}^{10} \sin k_y,$$

$$H_{1,10}^{+-} = 0,$$

$$H_{27}^{+-} = 2t_{27}^{10}(\cos k_x + \cos k_y),$$

$$H_{28}^{+-} = -2it_{29}^{10} \sin k_y,$$

$$H_{29}^{+-} = 2it_{29}^{10} \sin k_x,$$

$$H_{2,10}^{+-} = 2t_{2,10}^{10}(\cos k_x - \cos k_y),$$

$$\begin{aligned} H_{38}^{+-} &= 2t_{38}^{10} \cos k_x + 2t_{49}^{10} \cos k_y \\ &+ 2t_{38}^{21}[(\cos k_1 + \cos k_2)\cos k_x - (\sin k_1 - \sin k_2)\sin k_x] \\ &+ 2t_{49}^{21}[(\cos k_1 + \cos k_2)\cos k_y - (\sin k_1 + \sin k_2)\sin k_y], \end{aligned}$$

$$H_{39}^{+-} = 0,$$

$$H_{3,10}^{+-} = 2it_{4,10}^{10} \sin k_y,$$

$$\begin{aligned} H_{49}^{+-} &= 2t_{49}^{10} \cos k_x + 2t_{38}^{10} \cos k_y \\ &+ 2t_{49}^{21}[(\cos k_1 + \cos k_2)\cos k_x - (\sin k_1 - \sin k_2)\sin k_x] \\ &+ 2t_{38}^{21}[(\cos k_1 + \cos k_2)\cos k_y - (\sin k_1 + \sin k_2)\sin k_y], \end{aligned}$$

$$H_{4,10}^{+-} = 2it_{4,10}^{10} \sin k_x,$$

$$H_{5,10}^{+-} = 0. \tag{13}$$

H^{+-} is again real and hence

$$H^{+-} = H^{-+}. \tag{14}$$

In total, the block structure Eq. (5) specializes to

$$H = \begin{pmatrix} H^{++} & H^{+-} \\ H^{+-} & H^{++} \end{pmatrix}, \quad (H^{+-})^t = H^{+-}. \tag{15}$$

This Hamiltonian is easily block diagonalized. Consider the Bloch sums

$$\phi_{\boldsymbol{k}\nu}^{\pm i}(\boldsymbol{r}) = \sum_l e^{i\boldsymbol{k}\cdot(\boldsymbol{R}_l + \boldsymbol{S}_\pm)} \phi_i^{\pm}(\boldsymbol{r} - \boldsymbol{R}_l - \boldsymbol{S}_\pm),$$

$$i = 1, \ldots, 5, \tag{16}$$

with $\phi_i^{\pm}$ from Eq. (2) and form the combinations

$$\psi_{\boldsymbol{k}\nu}^{s/a,i} = \frac{1}{\sqrt{2}}(\phi_{\boldsymbol{k}\nu}^{+i} \pm \phi_{\boldsymbol{k}\nu}^{-i}), \tag{17}$$

where s stands for symmetric and a for alternating. Overlap of neighboring local orbitals is usually neglected in a tb approach.

If one, more generally, denotes with $\phi_i^{\pm}$ Wannier functions with the same crystal site symmetry as Eq. (7), then overlap in the original basis Eq. (7) is automatically included. This is done in all that follows. (See also next section.)

Then, Eq. (17) immediately yields

$$H^{ss} = H^{++} + H^{+-}, \quad H^{aa} = H^{++} - H^{+-}, \quad H^{sa} = 0 = H^{as}. \tag{18}$$

The next section deals with the determination of tb parameters from FPLO8 band structure results. Here, the tb model Eqs. (11)–(18) for the case of FeSe is analyzed as a typical example. The corresponding tb parameters are

$$t_{11}^{11} = 0.086, \quad t_{16}^{10} = -0.063,$$

$$t_{11}^{20} = -0.028, \quad t_{16}^{21} = 0.017,$$

$$t_{13}^{11} = -0.056i, \quad t_{18}^{10} = 0.305i,$$

$$t_{15}^{11} = -0.109, \quad t_{27}^{10} = -0.412,$$

$$\epsilon_1 = 0.014, \quad t_{22}^{11} = -0.066, \quad t_{29}^{10} = -0.364i,$$

$$\epsilon_2 = -0.539, \quad t_{23}^{11} = 0.089i, \quad t_{2,10}^{10} = 0.338,$$

$$\epsilon_3 = 0.020, \quad t_{33}^{11} = 0.232, \quad t_{38}^{10} = 0.080,$$

$$\epsilon_5 = -0.581, \quad t_{33}^{20} = 0.009, \quad t_{38}^{21} = 0.016,$$

$$t_{33}^{02} = -0.045, \quad t_{49}^{10} = 0.311,$$

$$t_{33}^{22} = 0.027, \quad t_{49}^{21} = -0.019,$$

$$t_{34}^{11} = 0.099, \quad t_{4,10}^{10} = 0.180i,$$

$$t_{35}^{11} = 0.146i \quad \text{all in eV}. \tag{19}$$

Only in a few cases the on-site energies ϵ_i and the hopping

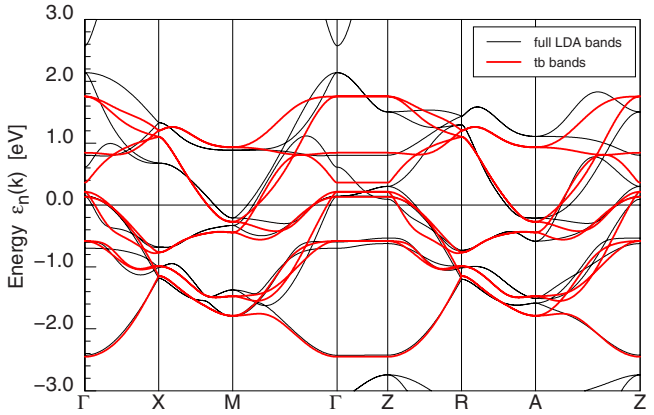

FIG. 10. (Color online) Comparison of the 2D tb bands with the full 3D LDA bands of FeSe.

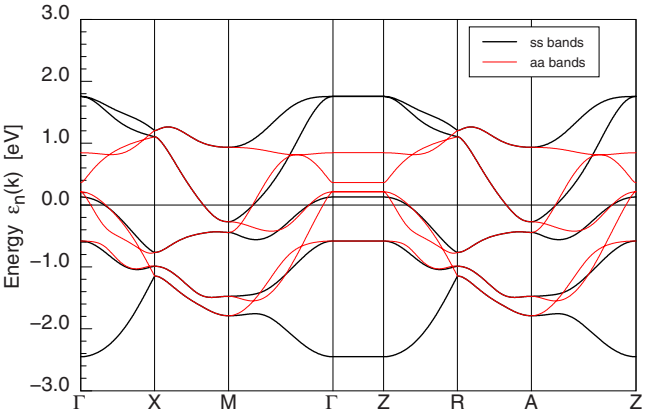

FIG. 12. (Color online) The ss- and aa-band groups corresponding to the Hamiltonian blocks Eq. (16) for FeSe.

matrix elements t directly obtained from the Wannier approach described in the next section are slightly renormalized in order to grossly account for the neglected hoppings to higher neighbors.

Figure 10 shows the obtained 2D two to five neighbor tb bands in comparison with the full LDA bands of the 3D FeSe crystal. For good reasons the focus of this treatment is on the vicinity of the Fermi level. On first glance it seems not to be an optimal fit there, in particular not around the points M and A (see Fig. 9 for M, the points Z, R, and A are at $k_z=\pi$ above Γ, X, and M). However, due to hybridization with the Se $4p$ states the Fe-Fe antibonding bands have a sizable k_z dispersion which cannot be provided by a 2D tb model. The quality on average of neglect of k_z dispersion of this tb model is also seen from the comparison of the DOS in Fig. 11 showing that the fit is not unreasonable close to the Fermi level.

A further feature of the 2D tb model is the block diagonalization (18) of the Hamiltonian matrix by means of lattice symmetry. There are two five-band groups in this model which do not interact in the whole BZ. One group comes from symmetric binary Wannier states (17) and one group from alternating ones. From what was said in the Introduction it follows that each of the two groups contains two Fe-Fe bonding and two Fe-Fe antibonding bands as well as one essentially nonbonding band. The two groups are shown in Fig. 12. Within each group there is no further decoupling in the whole BZ. In other words, a further reduction in the number of bands of a tb model necessarily demands inclusion of (many) higher than second neighbors to mimic the $\boldsymbol{k}$-dependent interaction with the omitted bands.

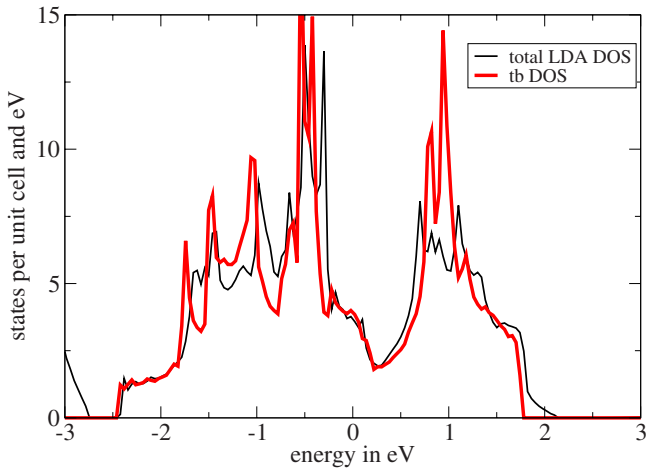

FIG. 11. (Color online) Comparison of the 2D tb DOS with the full 3D LDA DOS of FeSe.

On the side faces of the BZ the two groups are degenerate. As was demonstrated in Sec. II, this degeneracy is a general property of the $P4/nmm$ space group. It enables to fold out smoothly the ten bands into five bands in a doubled BZ (Jones zone).[17] One may chose the ss-bands in the BZ proper and the aa-bands folded out, or vice versa. It is now clearly seen that in any case this is not an out folding of antibonding bands against bonding bands. Were it so, a pseudogap between bonding and antibonding bands could not develop.

The other simplification, the reduction in a 10×10 Hamiltonian matrix to a matrix structure with two 5×5 blocks H^{++} (Hermitian) and H^{+-} (symmetric), is already guaranteed by Eq. (4) which holds for the 122 family too, for which there is no continuous outfolding. There is no additional benefit besides that.

In summary so far, without considerably worsening the fit, no less than the 27 tb parameters [Eq. (19)] will do in reasonably modeling the electronic structure of the iron chalcogenides/pnictides, even if one focuses on the Fermi level only. This is, unfortunately in stark contrast to the situation for the cuprates.

As can be inferred from Fig. 10(a) 2D tb fit for FeSe cannot be very satisfactory for quantitative studies even in an energy window of ±0.1 eV around the Fermi level, relevant for low temperature many-body approaches. This is different for the families 1111 and 122. In this respect, although their crystal structures are more complex their low-energy electronic structure is simpler and really distinctly 2D.

For LaOFeAs, the 2D tb parameters are obtained as

$$t_{11}^{11}=0.120, \quad t_{16}^{10}=-0.167,$$

$$t_{11}^{20}=-0.029, \quad t_{16}^{21}=0.027,$$

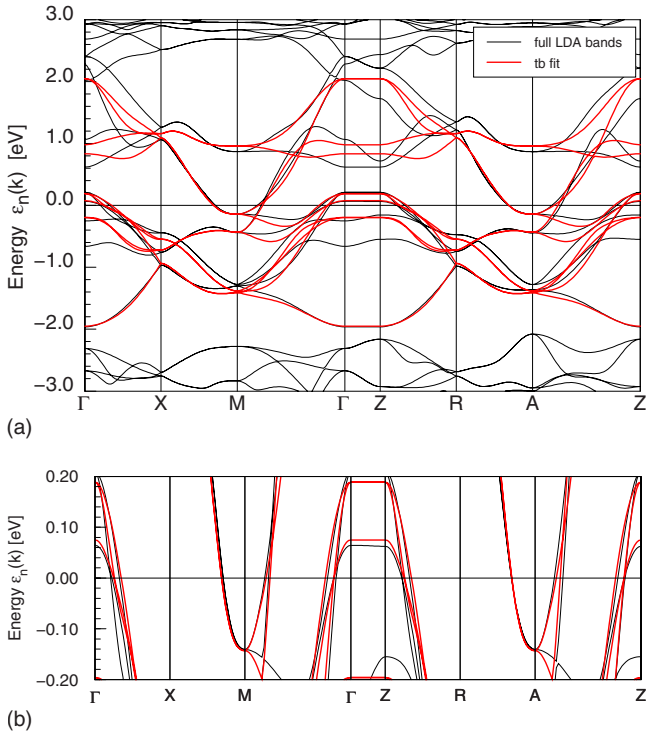

FIG. 13. (Color online) Comparison of the 2D tb bands with the full 3D LDA bands for LaOFeAs. (Top) full-energy window, (bottom) zoom in the low-energy region.

$$t_{13}^{11} = -0.014i, \quad t_{18}^{10} = 0.224i,$$

$$t_{15}^{11} = -0.172, \quad t_{27}^{10} = -0.348,$$

$$\epsilon_1 = 0.163, \quad t_{22}^{11} = -0.038, \quad t_{29}^{10} = -0.315i,$$

$$\epsilon_2 = -0.407, \quad t_{23}^{11} = 0.079i, \quad t_{2,10}^{10} = 0.296,$$

$$\epsilon_3 = 0.053, \quad t_{33}^{11} = 0.235, \quad t_{38}^{10} = 0.093,$$

$$\epsilon_5 = -0.196, \quad t_{33}^{20} = 0.023, \quad t_{38}^{21} = 0.026,$$

$$t_{33}^{02} = -0.025, \quad t_{49}^{10} = 0.335,$$

$$t_{33}^{22} = 0.032, \quad t_{49}^{21} = -0.008,$$

$$t_{34}^{11} = 0.094, \quad t_{4,10}^{10} = 0.126i,$$

$$t_{35}^{11} = 0.111i \quad \text{all in eV}. \tag{20}$$

The corresponding low-energy 2D bands are compared with the full 3D LDA bands in Fig. 13. Since here the FeAs layers are separated by LaO layers which have no states in the vicinity of the Fermi level, the full band structure has a pronounced 2D character there, and consequently the 2D tb approximation is of high quality. It does not need improvement by considering 3D dispersion. Nevertheless, for the LDA or GGA relaxed structure instead of the here considered experimental Wyckoff positions one of the z^2-derived bands crosses the Fermi level instead of the xy-derived one. This is why many published band structures show a hole pocket around Z instead of the third hole cylinder.

On the expense of an increase in the number of tb parameters to 44, of course a better overall fit of the 2D band structure in a larger energy window can be obtained.[3] Somewhat surprisingly, the situation for $BaFe_2As_2$ in a narrower energy window is similar although not equally perfect. This allows to treat the low-energy band structure of the 122 family within the same space group $P4/nmm$ (and BZ) which is the space group for one triple layer of FeAs, although the space group of the full 3D crystal is $I4/mmm$ (due to an n reflection of adjacently stacked FeAs triple layers). As a convenient consequence, the Hamiltonian Eqs. (11) and (13) with its simplifying block structure [Eq. (15)] applies.

The 2D tb parameters for $BaFe_2As_2$ are obtained as

$$t_{11}^{11} = 0.135, \quad t_{16}^{10} = -0.196,$$

$$t_{11}^{20} = -0.027, \quad t_{16}^{21} = 0.042,$$

$$t_{13}^{11} = -0.024i, \quad t_{18}^{10} = 0.218i,$$

$$t_{15}^{11} = -0.131, \quad t_{27}^{10} = -0.355,$$

$$\epsilon_1 = 0.172, \quad t_{22}^{11} = -0.131, \quad t_{29}^{10} = -0.365i,$$

$$\epsilon_2 = -0.236, \quad t_{23}^{11} = 0.103i, \quad t_{2,10}^{10} = 0.265,$$

$$\epsilon_3 = 0.000, \quad t_{33}^{11} = 0.204, \quad t_{38}^{10} = 0.065,$$

$$\epsilon_5 = -0.590, \quad t_{33}^{20} = 0.034, \quad t_{38}^{21} = 0.020,$$

$$t_{33}^{02} = -0.048, \quad t_{49}^{10} = 0.312,$$

$$t_{33}^{22} = 0.024, \quad t_{49}^{21} = -0.024,$$

$$t_{34}^{11} = 0.118, \quad t_{4,10}^{10} = 0.080i,$$

$$t_{35}^{11} = 0.078i \quad \text{all in eV}, \tag{21}$$

and the low-energy bands together with the full 3D LDA bands are shown in Fig. 14. (Note that we used the same path along the BZ as for the other cases, although the symmetry of the 122 system differs. This, however, facilitates comparison.)

Of course, in both Figs. 13 and 14 the tb bands on lines Γ-X-M-Γ and Z-R-A-Z are identical, but the full 3D LDA bands are not and the plot in particular also shows the distinct 2D character of the full bands and the quality of the 2D fit.

For later use we also give the 2D tb parameters for LiFeAs valid in connection with the Hamiltonian Eqs. (11) and (13) although without a 3D generalization provided in Sec. V the fit would not even qualitatively be correct. They are

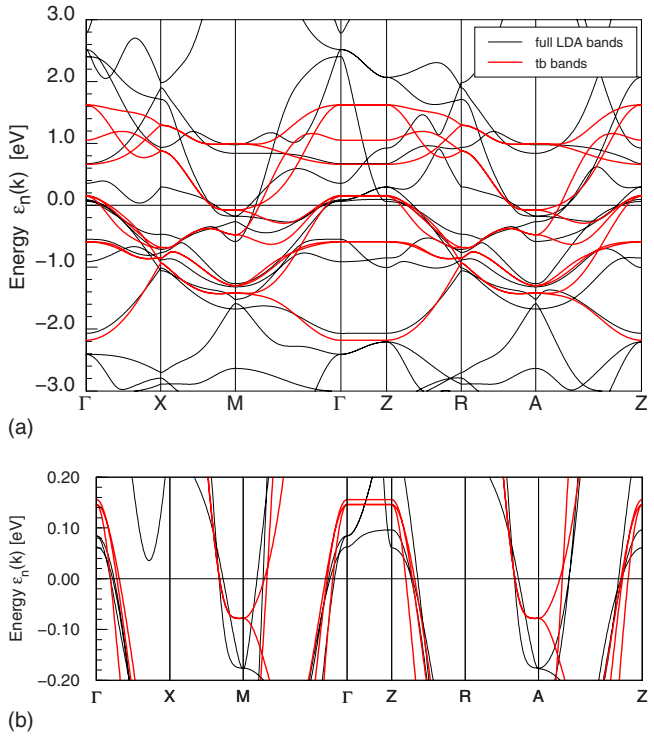

FIG. 14. (Color online) Like Fig. 12 for $BaFe_2As_2$. Above the Fermi level the full LDA bands are strongly hybridized with Ba 5*d* states.

$$t_{11}^{11}=0.079,\quad t_{16}^{10}=-0.016,$$

$$t_{11}^{20}=0.020,\quad t_{16}^{21}=0.013,$$

$$t_{13}^{11}=-0.090i,\quad t_{18}^{10}=0.281i,$$

$$t_{15}^{11}=-0.060,\quad t_{27}^{10}=-0.404,$$

$$\epsilon_1=-0.188,\quad t_{22}^{11}=-0.032,\quad t_{29}^{10}=-0.353i,$$

$$\epsilon_2=-0.521,\quad t_{23}^{11}=0.087i,\quad t_{2,10}^{10}=0.313,$$

$$\epsilon_3=0.200,\quad t_{33}^{11}=0.275,\quad t_{38}^{10}=0.125,$$

$$\epsilon_5=-0.609,\quad t_{33}^{20}=-0.002,\quad t_{38}^{21}=0.056,$$

$$t_{33}^{02}=-0.107,\quad t_{49}^{10}=0.359,$$

$$t_{33}^{22}=0.012,\quad t_{49}^{21}=-0.048,$$

$$t_{34}^{11}=0.102,\quad t_{4,10}^{10}=0.190i,$$

$$t_{35}^{11}=0.136i\quad \text{all in eV}. \tag{22}$$

IV. FPLO8 WANNIER FUNCTIONS

The determination of a Wannier function (WF) basis of states $|\boldsymbol{R}i\rangle$ with function index i at center $\boldsymbol{S}_i$ in unit cell $\boldsymbol{R}$, though formally being a simple Fourier transform of the Bloch states $|\boldsymbol{k}\nu\rangle$,

$$|\boldsymbol{R}i\rangle=\sum_{\boldsymbol{k},\nu}|\boldsymbol{k}\nu\rangle U_{\nu i}^{\boldsymbol{k}}e^{-i\boldsymbol{k}\cdot\boldsymbol{R}}, \tag{23}$$

becomes an art due to the inherent ambiguity of the choice of the band index and $\boldsymbol{k}$-vector dependent phase factors $U_{\nu i}^{\boldsymbol{k}}$.

There are basically three goals pursued, when calculating WFs, the first being to obtain functions, which form a suitable basis for the setup of model Hamiltonians. This aim usually implies that the resulting WFs should resemble basis functions, which have a certain chemical characteristic. The second goal is to reduce the degrees of freedom in the resulting model by projecting out high energy sectors resulting in few-band models. The last goal is to obtain model Hamiltonians with as few as possible parameters, which is essentially the requirement of maximal localization of the WFs. Reference 18 introduced a general method of calculating maximally localized WFs. Due to the nature of the problem at hand this approach is rather involved.

In order to fulfill the condition on the chemical characteristics it is in general desirable to pose symmetry restrictions on the WFs. In a local-orbital scheme with an optimized chemical basis set the basis orbitals usually show those characteristics, however, the resulting basis is nonorthogonal. Nevertheless, the local basis orbitals can be used as a starting point for the definition of WFs of a certain symmetry, which by construction have a high degree of localization.

We follow the ideas sketched in Ref. 19 and define a projection of the Bloch functions $|\boldsymbol{k}\nu\rangle$ onto local test functions $|\boldsymbol{S}i\rangle$. The resulting matrix elements $\langle\boldsymbol{k}\nu|\boldsymbol{S}i\rangle$ enter the phase factors $U_{\nu i}^{\boldsymbol{k}}$. They assign weights to the Bloch states entering the Fourier transform Eq. (23) such that the bands with the largest test function character contribute the most. It is very conceivable that optimized local basis orbitals are among the best possible choices of test functions. Thus in the simplest case we choose $|\boldsymbol{S}i\rangle$ to be a local orbital at the site $\boldsymbol{S}$ with orbital quantum numbers i. Alternatively, a linear combination of local orbitals [molecular orbital (MO)] centered at the WF center $\boldsymbol{S}$ could be used, in which case i denotes the characteristics of the MO.

The choice of the projector singles out all the bands exhibiting a particular character. In order to construct few-band models it is often desirable to additionally project out certain parts of the band complex with a particular character, say one is interested in WFs describing the antibonding part only. This is achieved by introducing energy windows described by functions $h_{\boldsymbol{S}i}(\epsilon_{\boldsymbol{k}\nu})$, which are basically unity in the relevant energy range and zero everywhere else.

All the projectors put together define the Bloch sums corresponding to the WFs

$$|\boldsymbol{k}i\}=|\boldsymbol{k}\nu\rangle h_{\boldsymbol{S}i}(\epsilon_{\boldsymbol{k}\nu})\langle\boldsymbol{k}\nu|\boldsymbol{S}i\rangle \tag{24}$$

which in general will be nonorthogonal. A subsequent symmetric orthogonalization defines the orthogonal WF Bloch sums.

$$|\boldsymbol{k}i\rangle = \sum_j |\boldsymbol{k}j\}(S^{-1/2})^{\boldsymbol{k}}_{ji}, \tag{25}$$

where $S^{\boldsymbol{k}}_{ji}=\{\boldsymbol{k}j|\boldsymbol{k}i\}$. The resulting phase factors

$$U^{\boldsymbol{k}}_{\nu i} = \sum_j h_{Sj}(\epsilon_{\mathbf{k}\nu})\langle \boldsymbol{k}\nu|\boldsymbol{S}j\rangle(S^{-1/2})^{\boldsymbol{k}}_{ji} \tag{26}$$

are then used in the Fourier transform Eq. (23) to calculate the WFs. They have predominately the character of the test functions $|\boldsymbol{S}i\rangle$ and approximate the bands which exhibit this character and lie in the chosen energy window. The WFs will transform according to the symmetry of the test functions. Due to the construction the largest part of the WF is actually formed by the test function itself. Since we use optimized chemical orbitals as test functions, the resulting WF will have a high degree of localization.

Furthermore, this construction results in WF band structures which do not only fit the band energies but also the orbital character of the bands. A band, which has predominantly a particular orbital character in the LDA bands will have the character of the corresponding Wannier function in the WF bands. Since the WFs are constructed to resemble the orbitals the Wannier character reflects the original orbital character. We confirmed this behavior explicitly by comparing orbital/WF projected bands.

In the present work, we used the Fe 3*d* orbitals as test functions. The energy window was chosen such that the c/p-4*p* bonding bands were excluded from the energy window and only the 10 Fe-dominated bands were included.

V. THREE-DIMENSIONAL DISPERSION

As indicated in Sec. III, there are reasons to consider the k_z dispersion close to the Fermi level in the family 11 and this becomes mandatory for the family 111. This increases the number of parameters considerably since it is connected with hopping through several layers, and, since there are no vertical bonds, each of these hoppings adds also one vector $\pm\boldsymbol{R}_1/2$ or $\pm\boldsymbol{R}_2/2$ (for hops from Fe to c/p) or $\pm\boldsymbol{T}_x$ or $\pm\boldsymbol{T}_y$ (for hops from c/p to c/p or to a cation).

In the 11 and 111 families, at least three hops are involved from an Fe layer to the next Fe layer (t^{rst} with $t=\pm 1$), and hence $t^{rs\pm 1}$ with $(r,s)=(0,0)$ or $(\pm 1,0)$ or $(0,\pm 1)$ or $(\pm 1,\pm 1)$ or $(\pm 2,0)$ or $(0,\pm 2)$ or $(\pm 1,\pm 2)$ or $(\pm 2,\pm 1)$ are of the same order of magnitude and have to be considered together. (Li or Na orbitals of the 111 family are not involved in the considered case.) For the vicinity of the Fermi level it suffices to consider the k_z dispersion of the *xy*, *xz*, and *yz* bands. The additions to the Hamiltonian matrix Eqs. (11) and (13) are ($k_z=\pi$ at BZ point *Z*)

$$H^{++}_{11} = H^{++}_{11} + [2t^{001}_{11} + 4t^{111}_{11}(\cos k_1 + \cos k_2) + 4t^{201}_{11}(\cos k_x + \cos k_y)]\cos k_z,$$

$$H^{++}_{13} = H^{++}_{13} - 4t^{201}_{14}\sin(2k_y)\sin k_z,$$

$$H^{++}_{14} = H^{++}_{14} - 4t^{201}_{14}\sin(2k_x)\sin k_z,$$

$$H^{++}_{33} = H^{++}_{33} + [2t^{001}_{33} + 4t^{201}_{33}\cos(2k_x) + 4t^{021}_{33}\cos(2k_y)]\cos k_z,$$

$$H^{++}_{44} = H^{++}_{44} + [2t^{001}_{33} + 4t^{021}_{33}\cos(2k_x) + 4t^{201}_{33}\cos(2k_y)]\cos k_z,$$

$$\begin{aligned} H^{+-}_{16} = H^{+-}_{16} &+ 4t^{101}_{16}(\cos k_x + \cos k_y)\cos k_z \\ &+ 2t^{121}_{16}\{[\cos(k_1+k_y)+\cos(k_1+k_x)]\exp(ik_z) \\ &+ [\cos(k_2+k_y)+\cos(k_2-k_x)]\exp(-ik_z)\}, \end{aligned}$$

$$\begin{aligned} H^{+-}_{18} = H^{+-}_{18} &- 4(t^{101}_{18}\sin k_x + t^{101}_{19}\sin k_y)\sin k_z \\ &+ 2it^{121}_{19}[\sin(k_1+k_y)\exp(ik_z) - \sin(k_2+k_y)\exp(-ik_z)], \end{aligned}$$

$$\begin{aligned} H^{+-}_{19} = H^{+-}_{19} &- 4(t^{101}_{19}\sin k_x + t^{101}_{18}\sin k_y)\sin k_z \\ &+ 2it^{121}_{19}[\sin(k_1+k_x)\exp(ik_z) - \sin(k_2-k_x)\exp(-ik_z)], \end{aligned}$$

$$\begin{aligned} H^{+-}_{38} = H^{+-}_{38} &+ 4(t^{101}_{38}\cos k_x + t^{101}_{49}\cos k_y)\cos k_z \\ &+ 2t^{121}_{38}[\cos(k_1+k_x)\exp(ik_z) + \cos(k_2-k_x)\exp(-ik_z)] \\ &+ 2t^{121}_{49}[\cos(k_1+k_y)\exp(ik_z) + \cos(k_2+k_y)\exp(-ik_z)], \end{aligned}$$

$$H^{+-}_{39} = H^{+-}_{39} + 4it^{101}_{39}(\cos k_x + \cos k_y)\sin k_z,$$

$$\begin{aligned} H^{+-}_{49} = H^{+-}_{49} &+ 4(t^{101}_{49}\cos k_x + t^{101}_{38}\cos k_y)\cos k_z \\ &+ 2t^{121}_{49}[\cos(k_1+k_x)\exp(ik_z) + \cos(k_2-k_x)\exp(-ik_z)] \\ &+ 2t^{121}_{38}[\cos(k_1+k_y)\exp(ik_z) + \cos(k_2+k_y)\exp(-ik_z)]. \end{aligned} \tag{27}$$

Since the Hamiltonian matrix is now complex, Eq. (15) does not hold anymore, but Eqs. (5) and (6) are still true.

For FeSe, of the 17 additional tb parameters contained in Eq. (27) the 14 non-negligible parameters are (again all in eV)

$$t^{101}_{16} = 0,$$

$$t^{001}_{11} = 0, \quad t^{211}_{16} = -0.017,$$

$$t^{111}_{11} = 0, \quad t^{101}_{18} = 0.009i,$$

$$t^{201}_{11} = 0.017, \quad t^{101}_{19} = 0.020i,$$

$$t^{201}_{14} = 0.030i, \quad t^{211}_{19} = 0.031i,$$

$$t^{001}_{33} = 0.011, \quad t^{101}_{38} = 0.006,$$

$$t^{201}_{33} = -0.008, \quad t^{211}_{38} = -0.003,$$

$$t^{021}_{33} = 0.020, \quad t^{101}_{39} = 0.015,$$

$$t^{101}_{49} = 0.025,$$

$$t^{101}_{49} = 0.006. \tag{28}$$

The comparison of the corresponding low-energy tb bands with the full LDA bands is shown in Fig. 15. The fit close to the Fermi level is probably about the best which can be

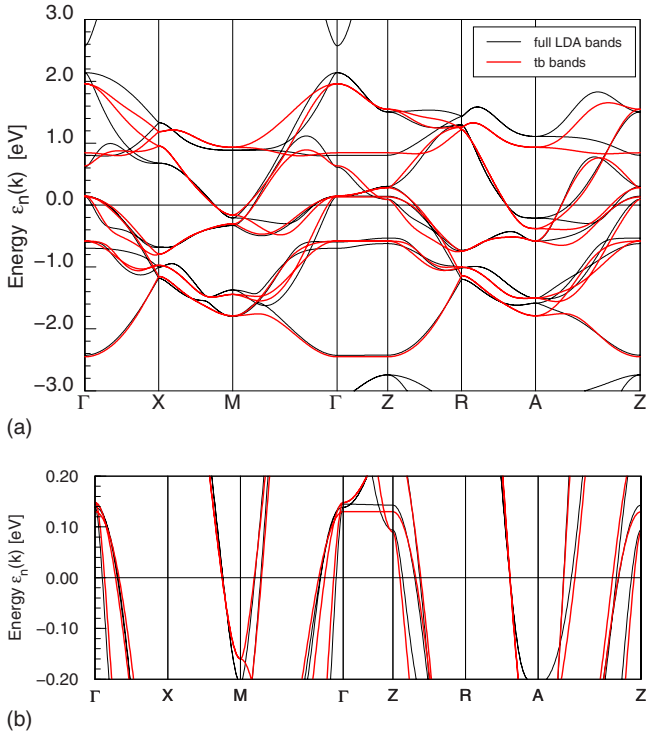

FIG. 15. (Color online) Comparison of the k_z-dispersed tb bands with the full LDA bands for FeSe. (Top) full-energy window, (bottom) zoom in the low-energy region.

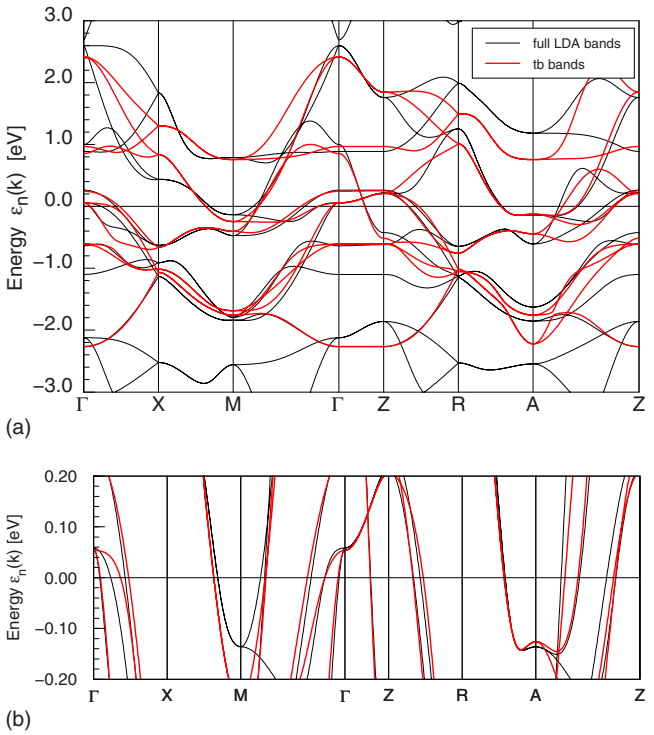

FIG. 16. (Color online) Like Fig. 15 for LiFeAs.

achieved in this case with a total of 41 parameters. The ten Fe-related bands of FeSe are separated from the rest of the bandstructure by gaps (see Figs. 2 and 6). If one takes the full set of several hundred of tb parameters calculated from our WFs, the fat (red) lines merge nearly perfectly the black ones in Fig. 10 for all ten Fe $3d$ related bands shown. This has been checked.

For LiFeAs, 16 of the 17 additional parameters contained in Eq. (27) are relevant. They are

$$t_{16}^{101} = -0.018,$$

$$t_{11}^{001} = 0.070, \quad t_{16}^{211} = -0.025,$$

$$t_{11}^{111} = 0.020, \quad t_{18}^{101} = 0.008i,$$

$$t_{11}^{201} = 0.005, \quad t_{19}^{101} = 0.020i,$$

$$t_{14}^{201} = 0.025i, \quad t_{19}^{211} = 0.022i,$$

$$t_{33}^{001} = -0.004, \quad t_{38}^{101} = 0,$$

$$t_{33}^{201} = -0.003, \quad t_{38}^{211} = -0.014,$$

$$t_{33}^{021} = 0.031, \quad t_{39}^{101} = 0.017,$$

$$t_{49}^{101} = 0.016,$$

$$t_{49}^{211} = 0.043. \tag{29}$$

The corresponding bands are compared with the full LDA bands in Fig. 16.

Besides the Fermi radii around M and A now being markedly different, there now appears a Fermi pocked around Γ with a FS crossing even the line Γ-Z. One radius around Γ could be improved on the expense of many more hopping parameters over larger distances only, which is again due to the far extension of the As $4p$ orbitals.

Let us finally shortly re-examine the 122 system. With a few z-hopping matrix elements, the tb fit in the wide-energy window shown in Fig. 14 cannot really be improved since the Ba $5d$ states, strongly hybridizing right above Fermi level, are very extended. Nevertheless, a few of those hoppings yield a better overall picture. The matrix elements in addition to Eq. (21) are

$$t_{11}^{101} = 0.061, \quad t_{16}^{001} = -0.161,$$

$$t_{14}^{\bar{2}11} = -0.029i, \quad t_{38}^{001} = 0.080,$$

$$t_{33}^{101} = 0.030, \quad t_{16}^{11\bar{1}} = -0.041. \tag{30}$$

Due to the different structure the additions to the Hamiltonian matrix are different from Eq. (27). They are

$$H_{11}^{++} = H_{11}^{++} + 2t_{11}^{101}(\cos k_x + \cos k_y)\cos k_z,$$

$$H_{13}^{++} = H_{13}^{++} + 2t_{14}^{\bar{2}11}[i \sin k_x \cos(2k_y)\cos k_z + \cos k_x \sin(2k_y)\sin k_z],$$

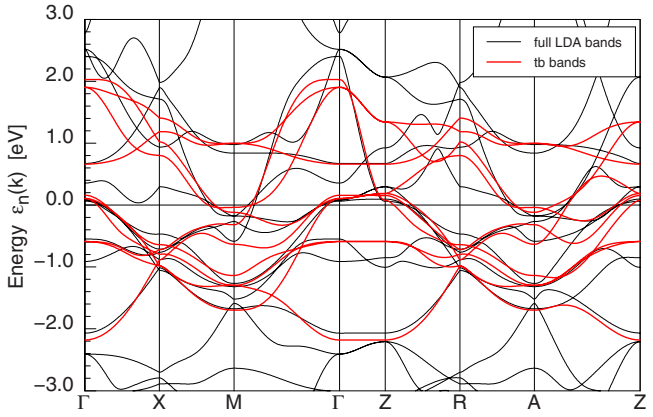

FIG. 17. (Color online) Comparison of a k_z dispersed 33 parameter tb fit of the Fe $3d$ bands with the full LDA bands for $BaFe_2As_2$.

$$H_{14}^{++} = H_{14}^{++} + 2\bar{t}_{14}^{211}[\sin(2k_x)\cos k_y \sin k_z + i\cos(2k_x)\sin k_y \cos k_z],$$

$$H_{33}^{++} = H_{33}^{33} + 4t_{33}^{101}\cos k_x \cos k_z,$$

$$H_{44}^{++} = H_{44}^{33} + 4t_{33}^{101}\cos k_y \cos k_z,$$

$$H_{16}^{+-} = H_{16}^{+-} + 2t_{16}^{001}\cos k_z + 2\bar{t}_{16}^{111}[\cos k_1 \exp(-ik_z) + \cos k_2 \exp(ik_z)],$$

$$H_{38}^{+-} = H_{38}^{+-} + 2t_{38}^{001}\cos k_z,$$

$$H_{38}^{+-} = H_{38}^{+-} + 2t_{38}^{001}\cos k_z. \quad (31)$$

This 3D tb fit is shown in Fig. 17. As is seen, there is one band (essentially of Ba $5d$ character) coming down close to the Fermi level which is not represented by the Fe $3d$ tb fit. At variance to the case of LiFeAs, here the 3D dispersing bands are, however, all unoccupied (and even move away from Fermi level under hole doping).

If one plays with the c/p-Wyckoff parameter or with larger ordered magnetic moments causing large additional exchange potentials and band shifts, the 3D behavior and maybe a FS crossing the line Γ-Z can reappear even for the 1111 and 122 families. This would put serious questions on the practicability of the tb approach at all, and one would probably have to go back to a full numerical WF treatment of the band structure.[20]

VI. CONCLUSIONS

We have demonstrated that the band structures of the nonmagnetic undoped iron-based superconductors for all four families have a quite complex multiorbital character with all 10 Fe $3d$ orbitals per unit cell involved in band states in a 0.1 eV vicinity of the Fermi level. Thereby, the states at the Fermi level are mainly of xz, yz, and xy character, respectively. However, departing from the Fermi level, the other Fe $3d$ orbitals and even the c/p-$4p$ orbitals start to hybridize and largely influence the Fermi velocities.

While the most investigated families 1111 and 122 exhibit clear 2D behavior in the low electronic energy regime, this is much less the case for the family 11 and not at all true for the family 111. Minimum quantitatively correct tb models are presented for FeSe, LiFeAs, LaOFeAs, and $BaFe_2As_2$ as representatives for the four families.

A minimum number of 27 tb parameters seems not to be reducible without severe loss of accuracy of the corresponding Fermi radii, Fermi velocities, and orbital character on the FS. For families 11 and 111 even that is not sufficient and the minimum number of tb parameters goes beyond 40.

ACKNOWLEDGMENTS

We benefited from discussions with Igor Mazin, Michelle Johannes, and Wei Ku.

*h.eschrig@ifw-dresden.de; http://www.ifw-dresden.de/~/helmut

[1] Y. Kamihara, T. Watanabe, M. Hirano, and H. Hosono, J. Am. Chem. Soc. **130**, 3296 (2008).

[2] M. Daghofer, A. Moreo, J. A. Riera, E. Arrigoni, D. J. Scalapino, and E. Dagotto, Phys. Rev. Lett. **101**, 237004 (2008); see also S. Graser, T. A. Maier, P. J. Hirshfeld, and D. J. Scalapino, Mem. Sci. Rev. Metall. **11**, 025016 (2009).

[3] K. Kuroki, S. Onari, R. Arita, H. Usui, Y. Tanaka, H. Kontani, and H. Aoki, Phys. Rev. Lett. **101**, 087004 (2008).

[4] F.-C. Hsu, J.-Y. Luo, K.-W. Yeh, T. K. Chen, T. W. Huang, P. M. Wu, Y. C. Lee, Y. L. Huang, Y. Y. Chu, D. C. Yan, and M. K. Wu, Proc. Natl. Acad. Sci. U.S.A. **105**, 14262 (2008); Y. Mizuguchi, F. Tomioka, S. Tsuda, T. Yamaguchi, and Y. Takano, Appl. Phys. Lett. **93**, 152505 (2008).

[5] X. C. Wang, Q. Q. Liu, Y. X. Lv, W. B. Gao, L. X. Yang, R. C. Yu, F. Y. Li, and C. Q. Jin, Solid State Commun. **148**, 538 (2008); C. W. Chu, F. Chen, M. Gooch, A. M. Guloy, B. Lorenz, B. Lv, K. Sasmal, Z. J. Tang, J. H. Tapp, and Y. Y. Hue, Physica C **469**, 326 (2009).

[6] P. Quebe, L. J. Terbuchte and W. Jeitschko, J. Alloys Comp. **302**, 70 (2000); Y. Kamihara, H. Hiramatsu, M. Hirano, R. Kawamura, H. Yanagi, T. Kamiya, and H. Hosono, J. Am. Chem. Soc. **128**, 10012 (2006); T. Watanabe, H. Yanagi, T. Kamiya, Y. Kamihara, H. Hiramatsu, M. Hirano, and H. Hosono, Inorg. Chem. **46**, 7719 (2007); T. M. McQueen, M. Regulacio, A. J. Williams, Q. Huang, J. W. Lynn, Y. S. Hor, D. V. West, M. A. Green, and R. J. Cava, Phys. Rev. B **78**, 024521 (2008); J. W. G. Bos, G. B. S. Penny, J. A. Rodgers, D. A. Sokolov, A. D. Huxley, and J. P. Attfield, Chem. Commun. (Camb.) 2008, 3634 (2008).

[7] M. Rotter, M. Tegel, and D. Johrendt, Phys. Rev. Lett. **101**, 107006 (2008).

[8] T. M. McQueen, Q. Huang, V. Ksenofontov, C. Felser, Q. Xu, H. Zandbergen, Y. S. Hor, J. Allred, A. J. Williams, D. Qu, J.

Checkelsky, N. P. Ong, and R. J. Cava, Phys. Rev. B **79**, 014522 (2009).
[9] K. Koepernik and H. Eschrig, Phys. Rev. B **59**, 1743 (1999).
[10] J. P. Perdew and Y. Wang, Phys. Rev. B **45**, 13244 (1992).
[11] I. I. Mazin, M. D. Johannes, L. Boeri, K. Koepernik, and D. J. Singh, Phys. Rev. B **78**, 085104 (2008).
[12] J. H. Tapp, Z. Tang, B. Lv, K. Sasmal, B. Lorenz, P. C. W. Chu, and A. M. Guloy, Phys. Rev. B **78**, 060505(R) (2008).
[13] C. de la Cruz, Q. Huang, J. W. Lynn, J. Li, W. Ratcliff II, L. Zarestky, H. A. Mook, G. F. Chen, J. L. Luo, N. L. Wang, and P. Dai, Nature (London) **453**, 899 (2008).
[14] M. Rotter, M. Tegel, D. Johrendt, I. Schellenberg, W. Hermes, and R. Pöttgen, Phys. Rev. B **78**, 020503(R) (2008).
[15] H. Eschrig and M. Richter, Solid State Commun. **59**, 861 (1986).
[16] *International Tables for Crystallography*, 4th ed., edited by T. Hahn (Kluwer, Dordrecht, 1995), Vol. A.
[17] H. Jones, *The Theory of Brillouin Zones and Electronic States in Crystals* (North-Holland, Amsterdam, 1960), Chap. 5, Sec. 42.1.
[18] N. Marzari and D. Vanderbilt, Phys. Rev. B **56**, 12847 (1997).
[19] Wei Ku, H. Rosner, W. E. Pickett, and R. T. Scalettar, Phys. Rev. Lett. **89**, 167204 (2002).
[20] Y. Yanagi, Y. Yamakawa, and Y. Ōno, J. Phys. Soc. Jpn. **77**, 123701 (2008).